

# Knowledge Distillation for Underwater Feature Extraction and Matching via GAN-synthesized Images

Jinghe Yang<sup>1</sup>, Mingming Gong<sup>2</sup>, and Ye Pu<sup>1</sup>

**Abstract**—Autonomous Underwater Vehicles (AUVs) play a crucial role in underwater exploration. Vision-based methods offer cost-effective solutions for localization and mapping in the absence of conventional sensors like GPS and LIDAR. However, underwater environments present significant challenges for feature extraction and matching due to image blurring and noise caused by attenuation, scattering, and the interference of *marine snow*. In this paper, we aim to improve the robustness of the feature extraction and matching in the turbid underwater environment using the cross-modal knowledge distillation method that transfers the in-air feature extraction models to underwater settings using synthetic underwater images as the medium. We first propose a novel adaptive GAN-synthesis method to estimate water parameters and underwater noise distribution, to generate environment-specific synthetic underwater images. We then introduce a general knowledge distillation framework compatible with different teacher models. The evaluation of GAN-based synthesis highlights the significance of the new components, i.e. GAN-synthesized noise and forward scattering, in the proposed model. Additionally, the downstream application of feature extraction and matching (VSLAM) on real underwater sequences validates the effectiveness of the transferred model.

## I. INTRODUCTION

Recently, Autonomous Underwater Vehicles (AUVs) have demonstrated great potential in underwater explorations, replacing human divers in hazardous and demanding scenarios. They are capable of performing various tasks, such as underwater facility repairs and inspections. Accurate localization and mapping are imperative for the successful execution of these missions, presenting a significant challenge due to the unavailability of in-air sensors like the Global Positioning System (GPS) and LIDAR in underwater environments. Consequently, AUVs have to depend on alternative sensors, such as cameras and sonar, for environmental perception and position estimation. Vision-based methods, which utilize cameras as sensing equipment, stand out for their affordability and ease of implementation [1].

Feature point extraction and matching is essential for deriving 3D geometric information from 2D images in applications like Structure-from-Motion (SfM) and Visual Simultaneous Localization and Mapping (VSLAM). Classical methods, such as SIFT [2] and ORB [3], are widely used; for instance, COLMAP [4] employs SIFT to identify correspondences between image frames for map reconstruction. Similarly, the ORB algorithm [3] is the front end of the ORB-SLAM [5] framework, facilitating camera motion

estimation across frames. Recently, learning-based methods have demonstrated significant potential in feature extraction and description [6], [7], [8], [9], particularly in challenging scenarios such as fast motion [10], underwater turbidity [11], and low-light environments [12].

Unlike in-air scenarios, where features are distinct, underwater features are often blurred and attenuated due to light absorption and scattering in water. These conditions pose significant challenges for feature extraction and matching in underwater imagery, as the performance of the feature extraction and description deteriorates rapidly with increasing turbidity [13]. This degradation adversely affects the robustness of downstream tasks. For instance, in [14], the authors compared the in-air feature-based VSLAMs, such as SVO [15] and ORB-SLAM2 [16], on underwater image sequences and observed frequent tracking loss under blurriness.

To enhance feature extraction and matching in blurry underwater images, several studies have implemented image restoration techniques to improve image quality and enhance the finding of feature correspondences [17], [18]. In [19], an additional classification model is used to mitigate incorrect feature detections on marine snow. Another promising approach involves cross-modal knowledge distillation. Earlier work, UFEN [11], leverages synthetic underwater images as a medium to transfer in-air feature extraction and matching knowledge to underwater scenarios. However, in UFEN, the synthetic images are generated using randomly sampled water parameters from various water types [20], with image noise simplified as white noise, limiting its adaptability to diverse underwater environments with varying characteristics.

The Generative Adversarial Network (GAN) [21] has been widely used in underwater image generation tasks to enhance the similarity between synthesized images and target underwater scenes, addressing the challenges of groundtruth collection in underwater environments. This approach serves as a precursor for various downstream tasks, including image restoration [22], [23], [24], [25] and depth estimation [26], [27]. However, synthetic images for feature extraction should account for not only color appearance in underwater environments but also critical factors such as blurring and image noise, which greatly impact the robustness of feature extraction and matching in underwater settings.

To address these challenges, we propose an adaptive GAN-based synthesis method integrated with a generalized knowledge distillation framework, enabling in-air feature extraction and description models to adapt to underwater scenarios. First, we propose a GAN-based approach that incorporates adaptive image noise distribution and forward scattering into

<sup>1</sup>Department of Electrical and Electronic Engineering, The University of Melbourne. <sup>2</sup>School of Mathematics and Statistics, The University of Melbourne.

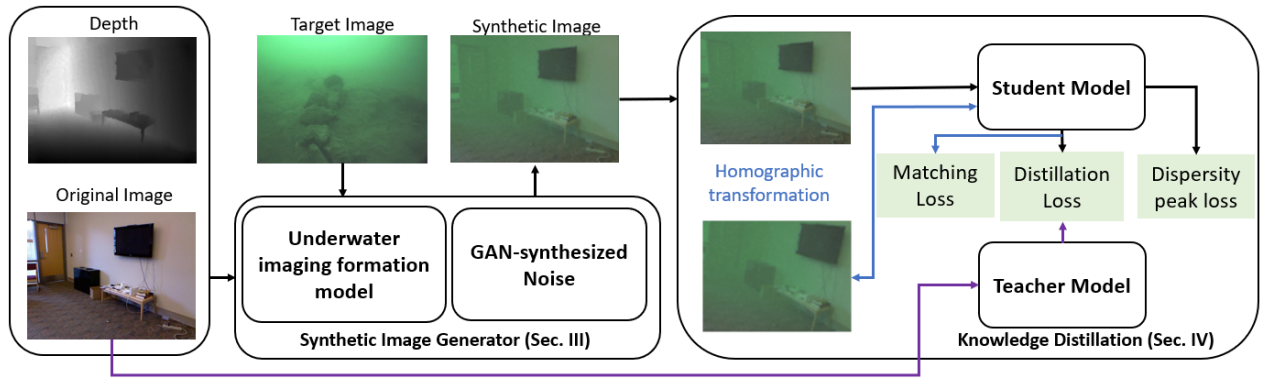


Fig. 1: **Overall training framework:** The training framework uses adaptive synthetic images of the target underwater environment as a medium to perform knowledge distillation from the in-air teacher model to the target underwater settings.

an image formation model to generate synthetic underwater images for the target environment (see Section III). Building upon previous work, we then present a framework that allows one to choose different in-air feature extraction networks as teacher models by introducing adaptation steps for different descriptor formats and dimensions (see Section IV). The overall framework is illustrated in Fig. 1. The key contributions of this paper are as follows:

- We present a GAN-based approach for synthesizing underwater images for specific environments, where the novelty lies in incorporating forward scattering and noise distribution in underwater image synthesis.
- We propose a general knowledge transfer framework, enabling knowledge distillation from different in-air teacher models to target underwater environments.
- We validate the effectiveness of our approach by integrating the transferred model into a VSLAM framework, improving robustness in challenging underwater environments.

## II. PRELIMINARIES

This section presents the preliminaries of this work, covering the background of the commonly used underwater imaging formation model, learning-based feature extraction and description, and underwater image synthesis.

### A. Underwater Imaging Formation Model

Underwater imaging differs greatly from in-air imaging. Recent studies have streamlined the underwater imaging model into two main components: the direct signal and the backscattering signal [28], [29], [30], [31]. The basic model can be expressed as:

$$I_c(x) = \underbrace{J_c(x) \cdot e^{-\beta_c z(x)}}_{\text{Direct Signal}} + \underbrace{B_c^\infty (1 - e^{-\beta_c z(x)})}_{\text{Backscattering}}, \quad (1)$$

here,  $I_c(x)$  and  $J_c(x)$  denote the intensities at pixel  $x$  in the captured underwater image and the unattenuated image, respectively, across the  $c \in \{R, G, B\}$  color channels. The direct signal describes photons traveling directly from objects to the camera, experiencing energy loss due to scattering and

absorption, with the attenuation rate determined by the beam attenuation coefficient  $\beta_c$  and the distance to the camera,  $z(x)$ . In contrast, backscattering is caused by the reflection of ambient light  $B_c^\infty$  from particles in water.

However, the basic model in (1) is overly simplified, overlooking characteristics of underwater imaging, such as forward scattering and the phenomenon known as marine snow. Marine snow, composed of organic material, detritus, and inorganic particles, plays a crucial role in underwater imaging. Its presence can lead to incorrect feature detections in underwater images [19] and inconsistent feature descriptions [11]. Modeling and synthesizing marine snow is particularly challenging due to its highly variable shapes and structures. Some studies address this challenge by employing mathematical models to simulate its behaviour [32], [33]. Furthermore, the motion blur caused by the movement of marine snow adds additional complexity to the synthesis.

This paper adopts the model in (1) as the foundation for synthetic image generation. The refined version of this model is introduced in Section III.

### B. Learning-based Feature Extraction and Description

In recent years, learning-based feature extraction and matching networks have demonstrated promising performance in identifying correspondences between image frames. Score map-based methods, which generate a score map to identify potential feature points and a descriptor map to assign vector descriptions to these points, represent one main category [34]. SuperPoint, proposed in [6], is trained starting from corner points on synthetic shapes and refined through a homographic adaptation strategy. R2D2 [9] focuses on discriminative learning the repeatability and reliability of features to achieve reliable detection and description. ALIKE [34] and ALIKED [8] utilize a differentiable key-point detection (DKD) and dispersivity peak loss for accurate and repeatable keypoint. Meanwhile, learning-based feature extraction methods have been employed to enhance the robustness of feature matching in challenging environments [10], [11]. The Underwater Feature Extraction Network (UFEN) [11] enhances feature extraction and matching from

blurry underwater images by generating synthetic images and applying cross-modal knowledge distillation

### C. Underwater Image Synthesis

Acquiring underwater ground truth is challenging for tasks like color restoration and depth estimation. To address this, synthetic underwater images are often used to build large underwater datasets [22], [26], [23]. The foundational approach leverages the underwater imaging formation model, using in-air RGB-D images with known water-type parameters to generate synthetic underwater images [11], [35]. The GAN method is an approach capable of synthesizing the target underwater environment. WaterGAN, proposed in [22], takes RGB-D images as input to generate synthetic underwater images by combining GAN methods with the underwater imaging formation model. These synthetic images serve as ground truth for image restoration tasks. Recent work [27] employs a diffusion model to generate diverse underwater scenes using in-air depth images as input, targeting underwater monocular depth estimation tasks.

## III. GAN-BASED IMAGE SYNTHESIS

In this section, we propose a model-based GAN approach used for underwater image synthesis, including the refined imaging formation model we employed and the GAN framework for estimating water parameters and noise distribution.

### A. Refined Underwater Imaging Formation Model

1) *Forward Scattering*: In the model (1), the forward scattering component, which describes light scattering at small angles biased toward the line of sight, is omitted, as its influence on image degradation is less than that of the other two components [36]. However, the existence of forward scattering causes blurriness in images, affecting feature detection and description. This scattering effect can be represented by the Point Spread Function (PSF) applied to the direct signal [37], [36]. Therefore we consider the following image model with forward scattering in this paper:

$$I_c(x) = \underbrace{(J_c * h_f)}_{\text{Forward Scattering}}(x) \cdot e^{-\beta_c z(x)} + B_c^\infty \cdot (1 - e^{-\beta_c z(x)}), \quad (2)$$

where PSF, denoted as  $h_f$ , is represented as a convolution blur kernel applied to the unattenuated scene image  $J_c$ . The convolution operator  $(*)$  is defined as:

$$(J_c * h_f)(x) = \sum_{x_i \in \mathcal{K}(x)} J_c(x_i) \cdot h_f(x, x_i), \quad (3)$$

with  $\mathcal{K}(x)$  representing the set of pixels in the kernel centered at  $x$ . The PSF can be expressed as a Gaussian function [38]:

$$h_f(x, x_i) = \kappa(x) \cdot \exp\left(-\frac{r(x, x_i)^2}{2\sigma(z(x))^2}\right), \quad (4)$$

where  $r(x, x_i)$  represents the pixel distance from  $x_i$  to the pixel  $x$  within the Gaussian kernel, and  $\sigma(z(x))$  is

the standard deviation dependent on the depth  $z(x)$ . The normalization factor  $\kappa(x)$  ensures that:

$$\sum_{x_i \in \mathcal{K}(x)} h_f(x, x_i) = 1. \quad (5)$$

Given that the radius of the Point Spread Function (PSF) in water increases linearly with distance, we define  $\sigma(z(x)) = \sigma_k \cdot z(x)$ , where  $\sigma_k$  is a trainable scalar factor controlling the effect of the PSF. We use a constant kernel size of 11 for overall images and perform normalization based on (5).

2) *Image Noise*: Image noise from marine snow in underwater environments affects feature extraction. A recent study [19] demonstrated that marine snow significantly impairs feature extraction performance. Moreover, the irregular motion of marine snow leads to inconsistent feature descriptions across image frames, thereby reducing feature-matching accuracy. Our synthesis process thus accounts for the image noise caused by marine snow, whose effect accumulates with increasing scene distance, similar to backscattering. We define the noise map  $M$ , which has the same dimensions as the image, applied to the pure backscattering background  $B_c^\infty$ . The backscattering background can be viewed as being partially filled with marine snow, represented as  $B_c^\infty(1 - M(x)) + M(x)$ . Here,  $M(x) \in [0, 1]$  represents a weight value at each pixel location  $x$ . We denote the additional image noise as  $B_c^{Noise}$ , formulated by:

$$B_c^{Noise}(x) = M(x)(1 - B_c^\infty)(1 - e^{-\beta_c z(x)}) \quad (6)$$

3) *Final Imaging Model*: Considering both forward scattering and image noise in the underwater environment,  $I_c^{Noise}$  represents the final obtained underwater image. We propose to use the following imaging formation model:

$$I_c^{Noise}(x) = I_c(x) + B_c^{Noise}(x), \quad (7)$$

where  $I_c$  and  $B_c^{Noise}$  are defined in (2) and (6), respectively.

### B. GAN Training Framework

1) *Framework Overview*: Natural underwater environments vary significantly in turbidity levels, color appearance and the distribution of the suspended particles. We propose a model-based GAN method to simulate the target environment to enhance knowledge distillation results for a specific environment. Underwater image synthesis for feature extraction purposes differs from restoration tasks [22], [24], [39], which focuses on color recovery while neglecting the effects of forward scattering and marine snow that influence feature extraction and matching. Moreover, it is crucial to avoid changing the positions of feature points during synthesis. Therefore we combine the proposed physical model with a neural-based generator in our generation process. The GAN generation framework is shown in Fig. 2.

2) *GAN Image Generation*: The GAN image generation consists of two components: the first generates images purely based on the physical imaging formation model, where the parameters  $\sigma_k$ ,  $\beta_c$ , and  $B_c^\infty$  in the imaging formation model (2) are trainable. This component produces smooth synthetic

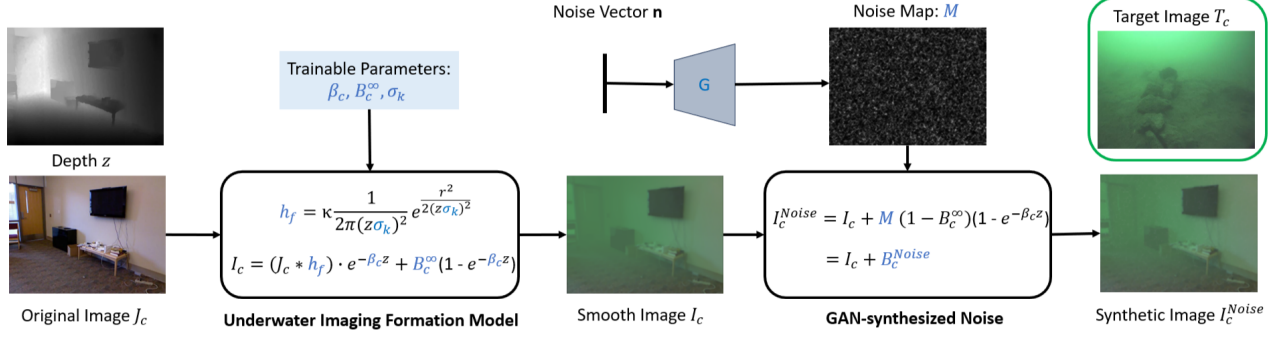


Fig. 2: **Synthetic Image Generation Framework:** This framework consists of two components: the underwater imaging formation model considering forward scattering and the GAN-synthesized image Noise.

images without noise (denoted as  $I_c$ ). The second component generates an estimate of the noise present in underwater images, including electronic noise from devices, uneven particle distributions in water, and marine snow. Since these types of noise are challenging to represent using a parameterized model, we use a neural-based generator  $G: \mathbb{R}^N \rightarrow \mathbb{M}$  to generate the noise map  $M \sim \mathbb{M}$  in (6), where  $\mathbf{n} \in \mathbb{R}^N$  is the random input vector of dimension  $N$ . This noise is then added to the smooth synthetic images to produce the final synthetic image ( $I_c^{Noise}$ ). To encourage the generated synthetic images to closely resemble the target underwater images, we adopt a modified LSGAN [40]. The discriminator  $D: \mathbb{I} \rightarrow [0, 1]$  takes both real images  $T_c \sim \mathbb{I}$  and synthetic images  $I_c^{Noise} \sim \mathbb{I}$  as input, where  $\mathbb{I}$  represents the image space. The training objectives are defined as follows:

$$\begin{aligned} \mathcal{L}_{gen} &= \mathbb{E}_{I_c^{Noise}} [(\mathbf{D}(I_c^{Noise}) - 1)^2], \\ \mathcal{L}_{disc} &= \mathbb{E}_{I_c^{Noise}} [\mathbf{D}(I_c^{Noise})^2] + \mathbb{E}_{T_c} [(\mathbf{D}(T_c) - 1)^2], \end{aligned} \quad (8)$$

where  $\mathcal{L}_{gen}$  is employed to update the trainable parameters in the physical imaging formation model ( $\sigma_k, \beta_c, B_c^\infty$ ) as well as the image noise generator  $G$ , while  $\mathcal{L}_{disc}$  denotes the loss function for the discriminator  $D$ .

3) *Evenly Distributed Noise Constraint:* Meanwhile, to ensure that the generated noise map  $M$  from  $G$  is evenly distributed across images, we introduce an additional discriminator  $D_d: \mathbb{R}^{m \times w \times h} \rightarrow [0, 1]$ , in which  $m$  is the batch

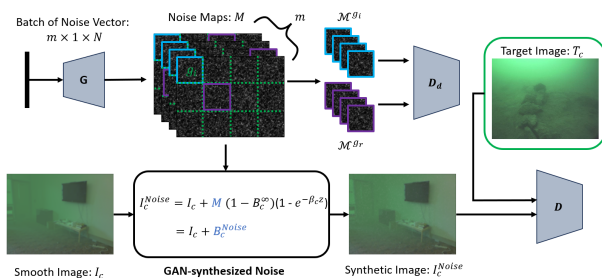


Fig. 3: **Training the Noise Generator G:** The training of the generator uses a discriminator  $D_d$  to ensure a uniform distribution of the generated noise map.

size,  $w$  and  $h$  are the grid size in width and height. Let  $\mathcal{G}$  denote the set of grid locations, uniformly sampled from the noise map  $M$ . For each batch of noise samples  $\mathcal{M} = \{M_1, M_2, \dots, M_m\}$ , with each  $M_j \sim \mathbb{M}$  ( $j = 1, \dots, m$ ), the discriminator compares patches sampled from the same grid location across the batch with patches sampled from random grid locations across all batch samples. Let  $g_i \in \mathcal{G}$  be the grid location on patch  $i$  ( $i = 1, \dots, \frac{HW}{hw}$ ),  $W$  and  $H$  are the image size in width and height. The batch of patches from the same grid location is denoted as:

$$\mathcal{M}^{g_i} = \{M_1^{g_i}, M_2^{g_i}, \dots, M_m^{g_i}\}, \quad g_i \in \mathcal{G}, \quad (9)$$

where  $M_j^{g_i}$  is the patch sampled from grid location  $g_i$  on the noise map  $M_j$ . Similarly, the batch of patches sampled from random grid locations across all samples is denoted as:

$$\mathcal{M}^{g_r} = \{M_1^{g_r}, M_2^{g_r}, \dots, M_m^{g_r}\}, \quad \{g_1, \dots, g_m\} \in \mathcal{G}. \quad (10)$$

This approach ensures that noise is evenly distributed across both individual images and batches. We denote  $\mathcal{M}^{g_r}$  as the batch of patches sampled from random grid locations and  $\mathcal{M}^{g_i}$  as the batch of patches sampled from fixed grid locations across samples. The distribution loss is defined as:

$$\begin{aligned} \mathcal{L}_{gen}^{dist} &= \mathbb{E}_{\mathcal{M}^{g_r}} [(\mathbf{D}_d(\mathcal{M}^{g_r}) - 1)^2], \\ \mathcal{L}_{disc}^{dist} &= \mathbb{E}_{\mathcal{M}^{g_r}} [\mathbf{D}_d(\mathcal{M}^{g_r})^2] + \mathbb{E}_{\mathcal{M}^{g_i}} [(\mathbf{D}_d(\mathcal{M}^{g_i}) - 1)^2], \end{aligned} \quad (11)$$

where  $\mathcal{L}_{disc}^{dist}$  is the loss function for the discriminator  $D_d$ . The final learning objective of the noise generator  $G$ , combined with  $\mathcal{L}_{gen}$  in (8), is to minimize:

$$\mathcal{L}_g = \mathcal{L}_{gen} + \lambda \mathcal{L}_{gen}^{dist}, \quad (12)$$

where  $\lambda$  is a weight parameter to balance the losses. The flow diagram for training  $G$  is shown in Fig. 3.

#### IV. ADAPTIVE KNOWLEDGE DISTILLATION FRAMEWORK FOR UNDERWATER FEATURE EXTRACTION

After generating synthetic underwater images, we perform knowledge distillation to transfer a pre-trained in-air feature extraction model to the underwater domain.

### A. Distillation loss

We perform the knowledge distillation step after generating synthetic images for a specific environment. The training framework for this process resembles that described in [11], which includes both the distillation loss from the extracted feature score map and the matching loss. We denote the feature score map and the corresponding descriptor map generated by the teacher model as  $\mathcal{X}^{Tea}$  and  $\mathcal{D}^{Tea}$ , and those by the student model as  $\mathcal{X}^{Stu}$  and  $\mathcal{D}^{Stu}$ . The knowledge distillation loss for the feature score map is defined as:

$$\mathcal{L}_{KD} = f_{\mathcal{X}}(\mathcal{X}^{Stu}, \mathcal{X}^{Tea}) + \alpha_{KD} f_{\mathcal{D}}(\mathcal{D}^{Stu}, \mathcal{D}^{Tea}), \quad (13)$$

where  $f_{\mathcal{X}}(\cdot)$  and  $f_{\mathcal{D}}(\cdot)$  represent the similarity loss functions used to compare the similarities between  $\mathcal{X}^{Tea}$  and  $\mathcal{X}^{Stu}$ , and  $\mathcal{D}^{Tea}$  and  $\mathcal{D}^{Stu}$ , respectively (e.g.,  $\mathcal{L}_2$  loss and Kullback-Leibler loss).  $\alpha_{KD}$  is a weight factor.

### B. Dispersity peak loss

To improve score precision at detected feature points, we apply the dispersity peak loss [34]. Given an image  $I_c^{Noise}$ ,  $N^{Stu}$  feature points  $x_i^{Stu}$  ( $i \in \{1, \dots, N^{Stu}\}$ ) are extracted using  $\mathcal{X}^{Stu}$ . For each feature point  $x_i^{Stu}$ , a local patch of size  $S \times S$  centered at  $x_i^{Stu}$  is defined and the *Softmax* [34] is applied to the score map within these patches. The pixel locations in the patch centered at  $x_i^{Stu}$  are denoted as  $x_{i,j}^{Stu}$ , where  $j \in \{1, 2, \dots, S^2\}$ , and the scores after *Softmax* at these pixels are denoted as  $s(x_{i,j}^{Stu})$ .  $r(x_i^{Stu}, x_{i,j}^{Stu})$  is the distance function, same to that in (4). Dispersity peak loss  $\mathcal{L}_{peak}$  is defined as:

$$\mathcal{L}_{peak} = \frac{1}{N^{Stu}} \sum_{i=1}^{N^{Stu}} \sum_{j=1}^{S^2} r(x_i^{Stu}, x_{i,j}^{Stu}) s(x_{i,j}^{Stu}). \quad (14)$$

### C. Matching loss

To ensure the matching performance of the descriptors, we use a matching loss  $\mathcal{L}_M$  to minimize the descriptor distance between matching feature points and maximize the descriptor distance between non-matching feature points. We apply a homographic transformation  $\mathcal{H}$  to the synthetic images  $I_c^{Noise}$  to obtain the image pair denoted as  $I_c^{\mathcal{H}}$ .  $N^{\mathcal{H}}$  matching feature are then extracted from  $I_c^{\mathcal{H}}$ , denoted as  $x_j^{\mathcal{H}}$ , where  $j \in \{1, 2, \dots, N^{\mathcal{H}}\}$ . The corresponding descriptors of the points,  $x_i^{Stu}$  and  $x_j^{\mathcal{H}}$  are denoted as  $d_i^{Stu}$  and  $d_j^{\mathcal{H}}$ . The matching loss is defined as:

$$\mathcal{L}_M = \frac{1}{Z^2 N^{\mathcal{H}}} \sum_{i=1}^{N^{Stu}} (p_i^2 + n_i^2), \quad (15)$$

where, for  $j \in \{1, 2, \dots, N^{\mathcal{H}}\}$ ,

$$\begin{aligned} p_i &= \max(0, \text{dist}(d_i^{Stu}, d_j^{\mathcal{H}}) - P), \\ n_i &= \max(0, Q - \text{dist}_n(d_i^{Stu}, d_j^{\mathcal{H}})), \end{aligned} \quad (16)$$

where  $Z$  is a scaling factor, equal to 1 for the float descriptor or to the descriptor dimension in the binary case. In (16),  $\text{dist}(\cdot)$  represents the descriptor distance between the matching descriptors  $d_i^{Stu}$  and the corresponding descriptor in the set  $d_j^{\mathcal{H}}$ , while  $\text{dist}_n(\cdot)$  represents the minimal descriptor

distance (e.g.,  $L_2$  distance) to the non-matching descriptors in  $d_j^{\mathcal{H}}$ .  $P$  and  $Q$  are two distance margins for the matching and non-matching descriptors, respectively. To accommodate the varying descriptor dimensions and formats across teacher models, we calculate the binary descriptor distance using the following equation:

$$\text{dist}(d_i^{Stu}, d_j^{\mathcal{H}}) = \frac{1}{2} (Z - d_i^{Stu} \cdot d_j^{\mathcal{H}}). \quad (17)$$

Meanwhile, same as the binarization step in UFEN [11], to prevent zero gradients during backpropagation in training, we employ the straight-through estimator.

### D. Final Loss

We use the weight parameters  $\gamma_1$  and  $\gamma_2$  to adjust the weights of the different training losses.

$$\mathcal{L} = \mathcal{L}_{KD} + \gamma_1 \mathcal{L}_{peak} + \gamma_2 \mathcal{L}_M \quad (18)$$

## V. EXPERIMENTS

In this section, we first evaluate the performance of the GAN-synthesized images through quantitative and qualitative analyses. Next, we assess models distilled from different teacher models, including SuperPoint and ALIKE, in terms of feature extraction and matching. Finally, we evaluate the transferred model on the downstream VSLAM task.

### A. Implementation Details

The training dataset for the GAN synthesis process consists of 1449 images from the NYU-v2 dataset [41], with 1149 images used for training and 300 for testing. The depth values are normalized between 0.5m and 5m to ensure scene consistency. We first perform the parameter estimation of the formation model in (2). The training is conducted with a batch size of 4 for 10k iterations. The learning rate is set to  $1 \times 10^{-3}$  for the trainable parameters and  $1 \times 10^{-4}$  for the discriminator  $\mathbf{D}$ , with updates occurring every 5 iterations. Then, the noise distribution estimation is performed with a batch size of 4 for 20k iterations. The learning rate is set to  $1 \times 10^{-5}$  for both the generator  $\mathbf{G}$  and the reinitialized discriminators  $\mathbf{D}$  and  $\mathbf{D}_d$ , with updates every 10 iterations, and  $\lambda$  is set to 0.1. The structure of the discriminators follows the multi-scale discriminators proposed in [42]. The generator, which is based on [43], replaces the encoder with a fully connected layer to adjust input random noise with size  $N = 5$  to the input size of the residual blocks and modifies the output layer to employ a *Sigmoid* activation function. In the knowledge distillation step, we continue using the dataset

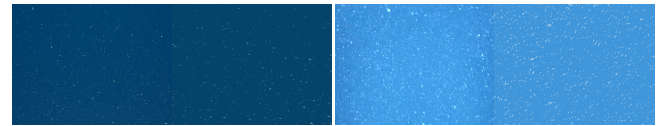
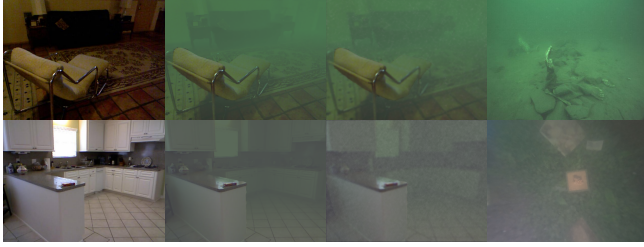


Figure 4: **Naive GAN Testing on Pure Background Images:** In the two displayed subsets, the left image represents the captured real image, while the right image is synthetic.



(a)  $J_c$  (b)  $I_c$  (c)  $I_c^{Noise}$  (d)  $T_c$

Fig. 5: **Qualitative Results on Synthetic Images:** Synthetic images are generated based on real target underwater images.

from the previous stage, training for 30 epochs. The learning rate is set to  $1 \times 10^{-5}$  for ALIKE and  $1 \times 10^{-6}$  for SuperPoint.  $\gamma_1$ ,  $\gamma_2$ , and  $\alpha_{KD}$  are set to 1, 1, and 0.01, respectively.

### B. GAN Synthetic Results

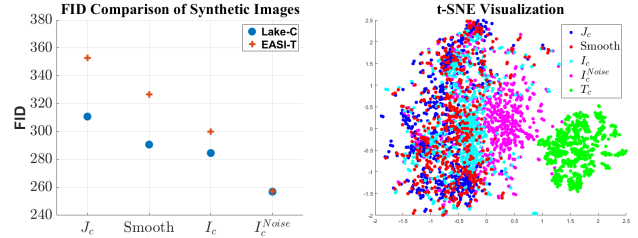
#### 1) Naive Case - Pure Underwater Background Synthesis:

To evaluate the performance of the GAN synthesis step, we first conduct a simple qualitative experiment where the target underwater images contain only the pure underwater background. In this scenario,  $J_c$  in (2) is set to 0, simplifying the formation model in (7) to:

$$I_c^{Pure}(x) = B_c^\infty + B_c^{Noise} = B_c^\infty(1 - M(x)) + M(x), \quad (19)$$

we extracted two distinct underwater environments from the marine snow dataset released in [19], which consists of footage with pure backgrounds, to serve as the target image  $T_c$ . The visual results from the GAN are displayed in Fig. 4. These findings confirm that our method produces a synthetic noise distribution akin to the marine snow in the target environment and accurately estimates the underwater background lights  $B_c^\infty$ . Therefore, our approach effectively estimates the underwater background lights and the noise distribution within the target environment.

2) *Target Underwater Image Synthesis:* To evaluate the complete synthesis of target environments, we selected two underwater sequences: the **EASI-T** sequence, sourced from the EASI dataset [11], which was created in an indoor water tank with baby powder used to adjust turbidity; and the **Lake-C** sequence, a simulated cemetery scene captured in a lake, sourced from [14]. Qualitative examples are shown in Fig. 5. We visually demonstrate the difference between the smooth synthetic images without GAN-synthesized noise and forward scattering and the fully synthetic images. To assess the effectiveness of each component in the synthesis process, we conducted a quantitative evaluation using the GAN metric Frchet Inception Distance (FID), where a lower score indicates a closer resemblance to the target images. We compared the FID scores of four groups against real underwater images: in-air RGB images ( $J_c$ ), smooth synthetic images without noise and forward scattering (Smooth), synthetic images without GAN noise ( $I_c$ ), and fully synthesized images ( $I_c^{Noise}$ ). Each group consisted of 500 randomly sampled images, with the results presented in Fig. 6. We



(a) FID scores (b) t-SNE visualization

Fig. 6: **Quantitative Evaluation on Synthesis Components:** With the addition of the synthesis components, the FID scores show a decreasing trend.

observe a decreasing trend in the FID scores as components are added, as illustrated in Fig. 6a. Using the EASI-T sequence as an example, we employed t-SNE to visualize the domain shift, which clearly shows a progression from left to right towards the target images in Fig. 6b. Notably, adding forward scattering and image noise components moves the synthetic images closer to the target domain.

### C. Feature Extraction and Matching Results

Using synthetic underwater images as the medium for knowledge distillation, the transferred model demonstrates enhanced performance in feature extraction on images from the target environment. To showcase the generalization of our training framework, we employ not only the SuperPoint [6] as the teacher model as in [11] but also the ALIKE model from [34] as the teacher model. We use the models to extract 500 feature points from  $480 \times 640$  images. Due to the lack of ground truth in real underwater sequences, we apply RANSAC to estimate the transformation between image frames with 5-image intervals and filter out mismatches. The performance of the models is evaluated using the Matching Number and the Matching Score metrics. Specifically, **Matching Num** (M. Num) is defined as  $N_{match}$ , which denotes the number of correct matches after RANSAC filtering, and **Matching Rate** (M. Rate) is given by  $N_{match}/N_{found}$ , where  $N_{found}$  represents the total number of matches identified using the descriptors. We randomly sample 100 image pairs from the sequences EASI-T and Lake-C and get the average, the evaluation results are shown in Table I. We use the **ALIKE(KD)** and **SuperPoint(KD)**

Models	Lake-C		EASI-T	
	M. Num	M. Rate	M. Num	M. Rate
ALIKE [34]	258.0	0.877	172.4	0.724
<b>ALIKE (KD)</b>	<b>264.0</b>	<b>0.929</b>	<b>220.5</b>	<b>0.844</b>
SuperPoint [6]	153.3	0.592	156.9	0.653
<b>SuperPoint (KD)</b>	<b>275.2</b>	<b>0.904</b>	<b>228.2</b>	<b>0.852</b>
UFEN [11]	244.2	0.807	184.6	0.692
<b>SuperPoint (KD-B)</b>	<b>246.6</b>	<b>0.861</b>	<b>205.1</b>	<b>0.821</b>

TABLE I: **Quantitative Evaluation on the Lake-C and EASI-T Sequences:** Both ALIKE(KD) and SuperPoint(KD) exhibit improved performance on their respective sequences. The binary model, SuperPoint(KD-B), outperforms UFEN.

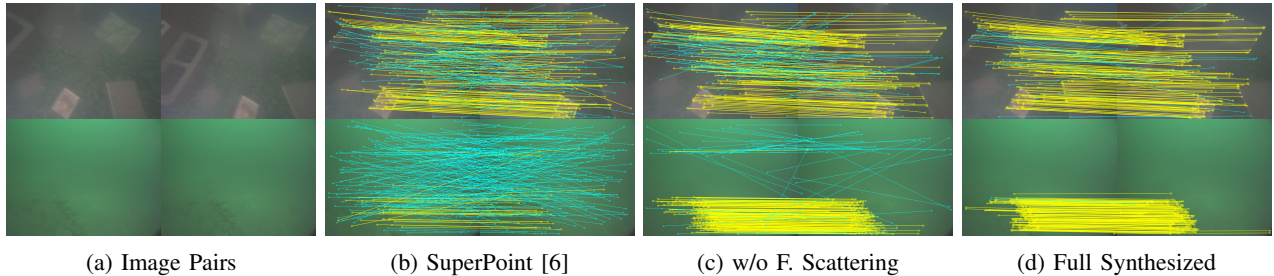


Fig. 7: **Qualitative Ablation Results on Feature Matching:** Correct matches (yellow), incorrect (blue). With the addition of GAN-synthesized noise and forward scattering, the number of incorrect matches is reduced.

to represent the models trained by our proposed knowledge distillation framework on the corresponding sequences. Additionally, to demonstrate the effectiveness of the proposed model and its performance compared to UFEN in [11], which was trained with randomly sampled water parameters and image white noise, we also performed knowledge distillation on SuperPoint with a binarization layer and the straight-through gradient estimator, labelled as **SuperPoint (KD-B)**, for a fair comparison with UFEN, whose descriptor is in binary format. The results demonstrate the effectiveness of our proposed knowledge distillation method. The general framework is versatile, working with different in-air feature extraction models and supporting various descriptor formats.

To evaluate the effectiveness of incorporating forward scattering and image noise in our synthetic image model, we conducted an ablation study using the knowledge-distilled SuperPoint model on the EASI-T sequence (Table II). Both Gaussian image noise (G. Noise) and GAN-synthesized noise (GAN Noise) enhance feature extraction and matching performance, with GAN Noise yielding superior results. Incorporating forward scattering (F. Scattering) further boosts performance. When both GAN-synthesized noise and forward scattering are considered, the model achieves the best performance. This study highlights the importance of accounting for forward scattering and image noise in underwater feature extraction and matching. Qualitative results in Fig. 7 further illustrate the effects of GAN-synthesized noise and forward

Synthetic Components			Performance Metrics	
G. Noise	GAN Noise	F. Scattering	M. Num	M. Rate
		✓	131.1	0.569
✓			166.9	0.727
✓		✓	175.3	0.755
	✓		193.2	0.756
	✓	✓	<b>228.2</b>	<b>0.852</b>

TABLE II: **Ablation study on the effect of forward scattering and noise map:** The best performance is achieved when both GAN noise and forward scattering are applied.

Seq.	ORB-SLAM3	UFEN-SLAM	Ours
Lake-C	11.9	82.1	100
EASI-T	0.0	9.7	100

TABLE III: **VSLAM Tracking Proportions (%):** UFEN-SLAM shows more robust performance on both sequences.

scattering in image synthesis. Matching correspondences are extracted using pure descriptor matching without RANSAC filtering. We compare the matching performance between the original SuperPoint model and the transferred model trained with synthetic images: one using only GAN noise (w/o F. Scattering) and another using fully synthesized images (Full Synthesized) with both components, where the proportion of incorrect matches is significantly reduced, especially in blurry and background regions.

#### D. Downstream Application: Underwater VSLAM Results

We further utilized the transferred feature extraction networks, trained using our method, in downstream VSLAM tasks. The knowledge distillation of the SuperPoint pre-trained model was performed using our GAN-synthesized images as the medium, with a binarization layer attached at the end of the descriptor. The model **SuperPoint KD-B** mentioned above, transferred through the GAN-synthesized images, was integrated into the front end of the ORB-SLAM3 framework, hereafter referred to as **Ours**, with descriptors converted into a 256-bit binary format to comply with the ORB-SLAM3 standard. The VSLAM performance on the real underwater sequence Lake-C is presented in Fig. 8. Due

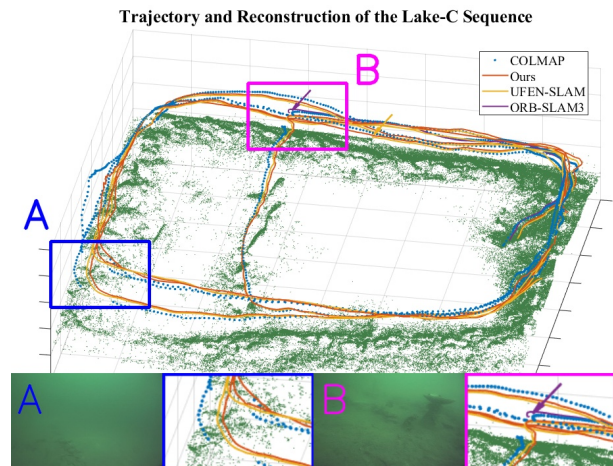


Fig. 8: **Visualization of VSLAM Results:** Our method, with enhanced features, tracks the full trajectory. COLMAP reconstruction has gaps in blurry regions, while UFEN-SLAM and ORB-SLAM3 fail to track the full trajectory.

to the absence of groundtruth for highly turbid underwater sequences, we utilized the Structure-from-Motion method, COLMAP, to reconstruct the Lake-C sequence. However, there are reconstructed frame gaps due to poor matching in blurry regions, as illustrated by image samples from scenes A and B, highlighting substantial reconstruction errors. Both ORB-SLAM3 and UFEN-SLAM failed to track the entire trajectory due to high turbidity and flowing particles, whereas our method maintained tracking throughout the sequence. Similar results were observed on the EASI-T dataset, where even ORB-SLAM3 was unable to initialize. The tracking proportions of these methods on the two sequences are summarized in Tab. III.

## VI. CONCLUSION

In this paper, we propose a knowledge distillation framework that transfers in-air feature extraction networks to underwater settings using adaptive GAN-synthesized images. Training on images that account for the forward scattering and image noise, our model outperforms ORB-SLAM3 and UFEN-SLAM on the VSLAM task.

## REFERENCES

- [1] A. Sahoo, S. K. Dwivedy, and P. S. Robi, "Advancements in the field of autonomous underwater vehicle," *Ocean Eng.*, vol. 181, 2019.
- [2] D. G. Lowe, "Distinctive image features from scale-invariant keypoints," *Int. J. Comput. Vis.*, vol. 60, 2004.
- [3] E. Rublee, V. Rabaud, K. Konolige, and G. Bradski, "Orb: An efficient alternative to sift or surf," in *Proc. IEEE Int. Conf. Comput. Vis. (ICCV)*, 2011.
- [4] J. L. Schonberger and J.-M. Frahm, "Structure-from-motion revisited," in *Proc. IEEE Conf. Comput. Vis. Pattern Recognit. (CVPR)*, 2016.
- [5] R. Mur-Artal and J. D. Tardós, "Orb-slam2: An open-source slam system for monocular, stereo, and rgb-d cameras," *IEEE Trans. Robot.*, vol. 33, no. 5, 2017.
- [6] D. DeTone, T. Malisiewicz, and A. Rabinovich, "Superpoint: Self-supervised interest point detection and description," in *Proc. IEEE/CVF Conf. Comput. Vis. Pattern Recognit. Workshops (CVPRW)*, 2018.
- [7] Z. Luo, L. Zhou, X. Bai, H. Chen, J. Zhang, Y. Yao, S. Li, T. Fang, and L. Quan, "Aslfeat: Learning local features of accurate shape and localization," in *Proc. IEEE/CVF Conf. Comput. Vis. Pattern Recognit. (CVPR)*, 2020.
- [8] X. Zhao, X. Wu, W. Chen, P. C. Y. Chen, Q. Xu, and Z. Li, "Aliked: A lighter keypoint and descriptor extraction network via deformable transformation," *IEEE Trans. Instrum. Meas.*, vol. 72, 2023.
- [9] J. Revaud, C. De Souza, M. Humenberger, and P. Weinzaepfel, "R2d2: Reliable and repeatable detector and descriptor," *Adv. Neural Inf. Process. Syst. (NeurIPS)*, vol. 32, 2019.
- [10] J. Tang, L. Ericson, J. Folkesson, and P. Jensfelt, "Gcnv2: Efficient correspondence prediction for real-time slam," *IEEE Robot. Autom. Lett. (RA-L)*, vol. 4, no. 4, 2019.
- [11] J. Yang, M. Gong, G. Nair, J. H. Lee, J. Monty, and Y. Pu, "Knowledge distillation for feature extraction in underwater vslam," in *Proc. IEEE Int. Conf. Robot. Autom. (ICRA)*, 2023.
- [12] Y. He, Y. Hu, W. Zhao, J. Li, Y.-J. Liu, Y. Han, and J. Wen, "Darkfeat: Noise-robust feature detector and descriptor for extremely low-light raw images," in *Proc. AAAI Conf. Artif. Intell. (AAAI)*, 2023.
- [13] K. Oliver, W. Hou, and S. Wang, "Image feature detection and matching in underwater conditions," in *Proc. SPIE Ocean Sens. Monit. II*, 2010.
- [14] B. Joshi, S. Rahman, M. Kalaitzakis, B. Cain, J. Johnson, M. Xanthidis, N. Karapetyan, A. Hernandez, A. Q. Li, and N. e. a. Vitzilaios, "Experimental comparison of open source visual-inertial-based state estimation algorithms in the underwater domain," in *Proc. IEEE/RSJ Int. Conf. Intell. Robots Syst. (IROS)*, 2019.
- [15] C. Forster, M. Pizzoli, and D. Scaramuzza, "Svo: Fast semi-direct monocular visual odometry," in *Proc. IEEE Int. Conf. Robot. Autom. (ICRA)*, 2014.
- [16] C. Campos, R. Elvira, J. J. G. Rodríguez, J. M. M. Montiel, and J. D. Tardós, "Orb-slam3: An accurate open-source library for visual, visual-inertial, and multimap slam," *IEEE Trans. Robot.*, vol. 37, no. 6, 2021.
- [17] Y. Cho and A. Kim, "Visibility enhancement for underwater visual slam based on underwater light scattering model," in *Proc. IEEE Int. Conf. Robot. Autom. (ICRA)*, 2017.
- [18] J. Xie, G. Hou, G. Wang, and Z. Pan, "A variational framework for underwater image dehazing and deblurring," *IEEE Trans. Circuits Syst. Video Technol.*, vol. 32, no. 6, 2021.
- [19] L. M. Hodne, E. Leikvoll, M. Yip, A. L. Teigen, A. Stahl, and R. Mester, "Detecting and suppressing marine snow for underwater visual slam," in *Proc. IEEE/CVF Conf. Comput. Vis. Pattern Recognit. (CVPR)*, 2022.
- [20] N. G. Jerlov, *Optical Oceanography*. Elsevier, 1968, vol. 5.
- [21] I. Goodfellow, J. Pouget-Abadie, M. Mirza, B. Xu, D. Warde-Farley, S. Ozair, A. Courville, and Y. Bengio, "Generative adversarial nets," *Adv. Neural Inf. Process. Syst. (NeurIPS)*, vol. 27, 2014.
- [22] J. Li, K. A. Skinner, R. M. Eustice, and M. Johnson-Roberson, "Watergan: Unsupervised generative network to enable real-time color correction of monocular underwater images," *IEEE Robot. Autom. Lett. (RA-L)*, vol. 3, no. 1, 2017.
- [23] C. Desai, R. A. Tabib, S. S. Reddy, U. Patil, and U. Mudenagudi, "Ruig: Realistic underwater image generation towards restoration," in *Proc. IEEE/CVF Conf. Comput. Vis. Pattern Recognit. (CVPR)*, 2021.
- [24] J. Wen, J. Cui, Z. Zhao, R. Yan, Z. Gao, L. Dou, and B. M. Chen, "Syreanet: A physically guided underwater image enhancement framework integrating synthetic and real images," in *Proc. IEEE Int. Conf. Robot. Autom. (ICRA)*, 2023.
- [25] M. J. Islam, Y. Xia, and J. Sattar, "Fast underwater image enhancement for improved visual perception," *IEEE Robot. Autom. Lett. (RA-L)*, vol. 5, no. 2, 2020.
- [26] P. Hambarde, S. Murala, and A. Dhall, "Uw-gan: Single-image depth estimation and image enhancement for underwater images," *IEEE Trans. Instrum. Meas.*, vol. 70, 2021.
- [27] F. Zhang, S. You, Y. Li, and Y. Fu, "Atlantis: Enabling underwater depth estimation with stable diffusion," in *Proc. IEEE/CVF Conf. Comput. Vis. Pattern Recognit. (CVPR)*, 2024.
- [28] D. Akkaynak and T. Treibitz, "A revised underwater image formation model," in *Proc. IEEE Conf. Comput. Vis. Pattern Recognit. (CVPR)*, 2018.
- [29] J. Y. Chiang and Y.-C. Chen, "Underwater image enhancement by wavelength compensation and dehazing," *IEEE Trans. Image Process.*, vol. 21, no. 4, 2011.
- [30] Y.-T. Peng, X. Zhao, and P. C. Cosman, "Single underwater image enhancement using depth estimation based on blurriness," in *Proc. IEEE Int. Conf. Image Process. (ICIP)*, 2015.
- [31] J. Yang, M. Gong, and Y. Pu, "Physics-informed knowledge transfer for underwater monocular depth estimation," in *Proc. Eur. Conf. Comput. Vis. (ECCV)*, 2024.
- [32] M. Boffety and F. Galland, "Phenomenological marine snow model for optical underwater image simulation: Applications to color restoration," in *Proc. Oceans-Yeosu*, 2012.
- [33] R. Kaneko, Y. Sato, T. Ueda, H. Higashi, and Y. Tanaka, "Marine snow removal benchmarking dataset," in *Proc. APSIPA ASC*, 2023.
- [34] X. Zhao, X. Wu, J. Miao, W. Chen, P. C. Y. Chen, and Z. Li, "Alike: Accurate and lightweight keypoint detection and descriptor extraction," *IEEE Trans. Multimedia*, vol. 25, 2022.
- [35] G. Hou, X. Zhao, Z. Pan, H. Yang, L. Tan, and J. Li, "Benchmarking underwater image enhancement and restoration, and beyond," *IEEE Access*, vol. 8, 2020.
- [36] Y. Y. Schechner and N. Karpel, "Clear underwater vision," in *Proc. IEEE Conf. Comput. Vis. Pattern Recognit. (CVPR)*, 2004.
- [37] J. S. Jaffe, "Computer modeling and the design of optimal underwater imaging systems," *IEEE J. Ocean. Eng.*, vol. 15, no. 2, 1990.
- [38] X. Zhu and P. Milanfar, "Image reconstruction from videos distorted by atmospheric turbulence," in *Proc. SPIE Vis. Inf. Process. Commun.*, 2010.
- [39] S. Liu, H. Fan, S. Lin, Q. Wang, N. Ding, and Y. Tang, "Adaptive learning attention network for underwater image enhancement," *IEEE Robot. Autom. Lett. (RA-L)*, vol. 7, no. 2, 2022.
- [40] X. Mao, Q. Li, H. Xie, R. Y. K. Lau, Z. Wang, and S. Paul Smolley, "Least squares generative adversarial networks," in *Proc. IEEE Int. Conf. Comput. Vis. (ICCV)*, 2017.

- [41] N. Silberman, D. Hoiem, P. Kohli, and R. Fergus, "Indoor segmentation and support inference from rgb-d images," in *Proc. Eur. Conf. Comput. Vis. (ECCV)*, 2012.
- [42] T.-C. Wang, M.-Y. Liu, J.-Y. Zhu, A. Tao, J. Kautz, and B. Catanzaro, "High-resolution image synthesis and semantic manipulation with conditional gans," in *Proc. IEEE Conf. Comput. Vis. Pattern Recognit. (CVPR)*, 2018.
- [43] X. Huang, M.-Y. Liu, S. Belongie, and J. Kautz, "Multimodal unsupervised image-to-image translation," in *Proc. Eur. Conf. Comput. Vis. (ECCV)*, 2018.